minerals

MDPI

Article

Coupling Mechanism of the Concealed Rock Body and Metallogenic Structure of the Sarakan Gold Deposit in Laos Investigated Using Magnetic and Electrical Methods

Hui Li [1], Jie Gan [2,3,*], Yu Gan [4], Bin Wang [1,4], Yong Li [4] and Wei Jiang [4]

[1] College of Earth Science, Chengdu University of Technology, Chengdu 610059, China; lihui@stu.cdut.edu.cn (H.L.); wangbin3088@163.com (B.W.)
[2] College of Geophysical, Chengdu University of Technology, Chengdu 610059, China
[3] Geological Resources and Geological Engineering Postdoctoral Workstation, Chengdu University of Technology, Chengdu 610059, China
[4] The 7th Geological Team of the Bureau of Geological and Mineral Resources of Sichuan, Leshan 614000, China; 13990657092@163.com (Y.G.); lyuyun515@163.com (Y.L.); 13890618175@163.com (W.J.)
* Correspondence: ganjie@cdut.edu.cn

Abstract: The Sarakan Gold Deposit is located in the vicinity of the Songsanu and Napafa villages, north of Sarakan County, Vientiane Province, Laos. It forms part of the Luang Prabang–Loei polymetallic metallogenic belt, and its metallogenic geological conditions are good and mineral resources are abundant. At present, most orebodies (mineralization) are deeply buried and greatly vary in terms of their characteristics; furthermore, the distribution and output of orebodies (mineralization) are not clear, which makes it difficult to find minerals in the area. Based on the comprehensive geological characteristics, geophysical anomalies, and interpretation results in the study area, it is believed that the Sarakan Gold Deposit is closely related to Indosinian felsic substance magmatic intrusions and is controlled by their structure. The type of deposits in the belt are brittle–ductile, shear structured, Quartz-pyrite, vein-type gold deposits. In this study, we carried out comprehensive geophysical methods, including the high-precision magnetic survey, induced polarization survey, and the transient electromagnetic measurement. Based on the characteristics of geophysical anomalies, geological inference, and interpretation, the integrated geophysical and geochemical prospecting criteria of the ore area have been determined: high magnetism, high polarization, and medium–high resistance are the signs pointing to concealed mineralization bodies in the study area, and this provided the best framework for us to discuss the deep geological bodies in the study area. The drilling verification results are consistent with the abnormalities delineated by the magnetic and electrical measurements. Our geophysical exploration results revealed the coupling relationship between the concealed intrusive body of the Sarakan Gold Deposit and the metallogenic structure, which provided a great opportunity for finding potentially similar deposits in the Luang Prabang–Loei polymetallic metallogenic belt.

Keywords: geophysical investigation; polymetallic deposit; magnetic exploration; IP measurement; Luang Prabang–Loei island arc belt; Laos

check for updates

Citation: Li, H.; Gan, J.; Gan, Y.; Wang, B.; Li, Y.; Jiang, W. Coupling Mechanism of the Concealed Rock Body and Metallogenic Structure of the Sarakan Gold Deposit in Laos Investigated Using Magnetic and Electrical Methods. *Minerals* **2023**, *13*, 912. https://doi.org/10.3390/min13070912

Academic Editors: Fuhao Xiong, Bin Liu and Paul Alexandre

Received: 28 April 2023
Revised: 25 June 2023
Accepted: 4 July 2023
Published: 6 July 2023

Copyright: © 2023 by the authors. Licensee MDPI, Basel, Switzerland. This article is an open access article distributed under the terms and conditions of the Creative Commons Attribution (CC BY) license (https://creativecommons.org/licenses/by/4.0/).

1. Introduction

In recent years, magnetic methods have been widely used to detect concealed rock bodies, orebodies, and underground structures [1–4]. Further, the induced polarization (IP) method is a relatively mature geophysical exploration method for finding sulfide mineral deposits [5,6]. It has a high working efficiency, fast surface-sweeping speed, and is relatively unaffected by topography [7–9]. The ores or mineralized bodies and surrounding rocks in the area have differing magnetic properties and electrical parameters, which indicates that there are certain prerequisites for the development of magnetic and

IP methods, and the delineated magnetic anomalies and IP anomalies can be regarded as good prospecting signs.

The southwestern part of Laos and its neighboring areas are rich in mineral resources. There exists an important copper-gold-silver polymetallic metallogenic belt in the Indochina Peninsula, which has significant exploration potential [10–15]. The Sarakan Gold Deposit is located in the northern part of the Luang Prabang–Loei volcanic arc belt. It is affected by the previous tectonic movements, since the Jinning movement [16]. Each stage of tectonic movement is accompanied by volcanic activity and the corresponding tectonic system and metallogenic activity, and they are superimposed on each other [9,17–19]. It provides good geological conditions for the formation of various minerals and is the best area to find copper-gold-silver polymetallic deposits [20]. The Newmont Company, in the United States, has carried out water-system geochemical and aerial geophysical surveys in northwestern Laos, and believes that the Sarakan area contains significant amounts of gold, copper, lead, zinc, silver, and other precious metals under non-ferrous metal metallogenic conditions. There is a huge potential for large gold deposits. Owing to the low degree of geological prospecting and geological research in Laos, basic theoretical problems such as the evolution of the geological structure and the law of mineralization in the study area have not been sufficiently investigated [8,21–23]. Although a small number of Au-Ag-Cu orebodies and a low amount of mineralization have been discovered in the study area, the shallow orebodies on the surface are smaller in scale and lower in taste [24–26]. Therefore, it is necessary to carry out comprehensive and systematic prospecting work in the deep portions of the study area [27,28].

2. Regional Geology

The Sarakan Gold Deposit is located in southwestern Laos. In terms of the tectonic unit, it is located in the Luang Prabang–Loei volcanic island arc zone (level IV), to the northwest of the Indochina block (level III) (Figure 1). The Indochina block lies in the South China Sea, on the southwestern margin of the Asian continental plate (level II) in the Tethys-Himalayan tectonic domain (level I) [16]. It is the southern extension of the Sanjiang passive continental margin structural belt in southwest China, which has a significant metallogenic background [29–33]. Under the influence of two large regional fault zones (F3 and F4), the overall structure of the region manifests as broad and gentle compound folds and faults, dominant in the NNE direction. The regional outcropping strata are mainly Upper Carboniferous–Upper Permian and Quaternary. The main magmatic rock is the Bansacay group, which cuts through the Late Carboniferous–Early Permian carbonate–terrigenous deposits and the Late Permian basalt–andesite. It is mainly composed of a combination of diorite–granodiorite–quartz monzonite–granite. According to Li et al. [34], the zircon U-Pb age of magmatic rocks obtained from the Nanpo Gold Deposit in the Sarakan area is 248 Ma, indicating that a large-scale intermediate-acid magmatic intrusion occurred in the early Indosinian period. Previous research results have shown that the gold deposits in the Luang Prabang–Loei island arc are closely related to Indosinian meso-acid magmatic rocks, and most of these deposits are quartz vein-type rock gold deposits of mesothermal–hydrothermal origin. Under the control of the regional structure, the ore bodies are mainly produced in the form of veins in the structural shear zone and the structural fracture zone [35–37].

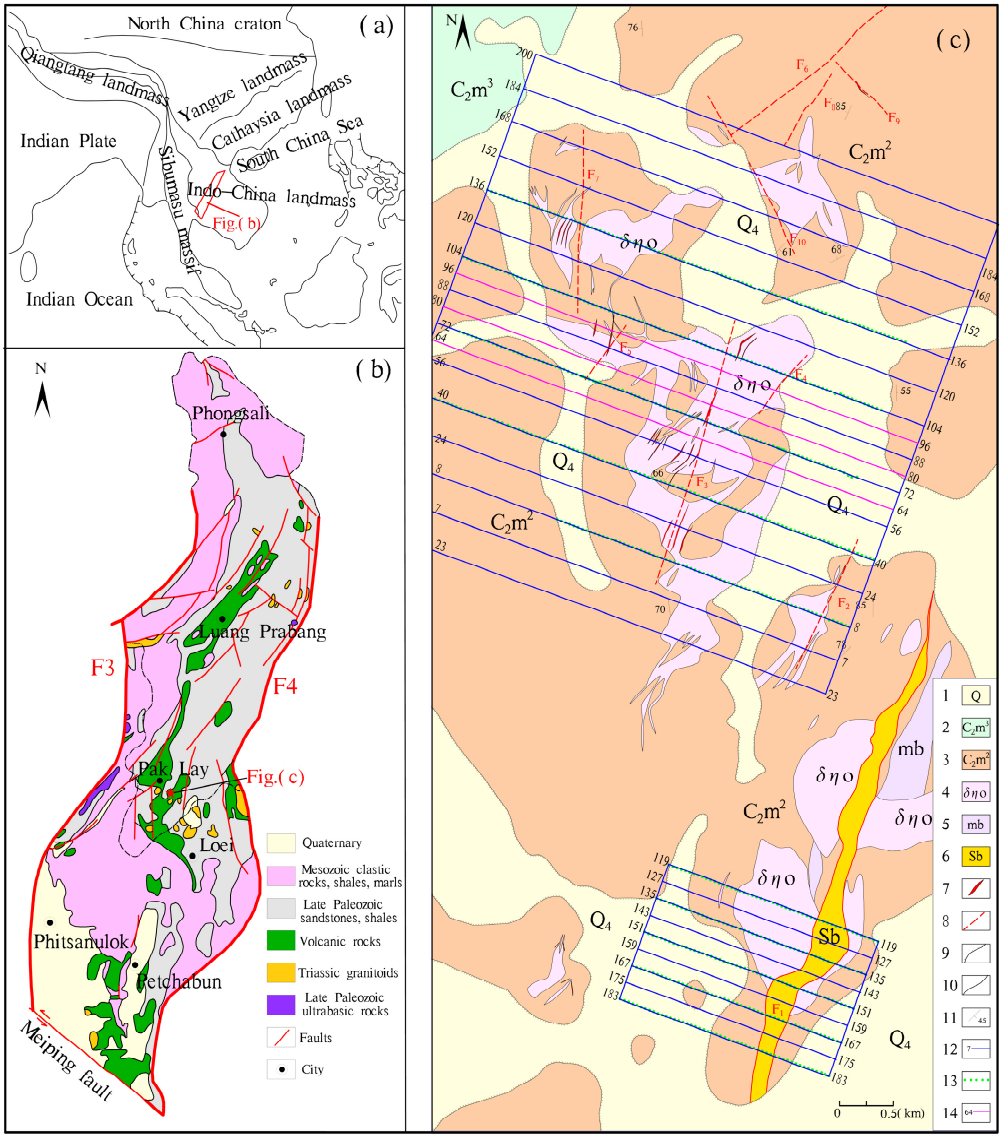


Figure 1. (**a**) Geotectonic location map of Luang Prabang–Loei metallogenic belt. (**b**) Geological diagram of Luang Prabang–Lee metallogenic belt. (**c**) Geological diagram of Sarakan Gold Deposit in Laos. 1. Quaternary alluvial strata and residual strata; 2. The third member of Mengnan County Formation; 3. The second member of Mengnan County Formation; 4. Quartz monzonite; 5. Marble; 6. Fault fracture zone; 7. Gold orebody; 8. Fault; 9. Angle unconformity boundary; 10. Measured geological boundary; 11. Occurrence; 12. Geophysical survey line and number; 13. Transient electromagnetic measuring points; 14. Magnetic survey line and number.

3. Geological and Geophysical Characteristics of the Deposit

3.1. Geological Characteristics of the Deposit

Through geological mapping, it was determined that the stratum of the mining area is mainly the Upper Carboniferous (C_2), above which is an intermittent Quaternary (Q_4) alluvial-slope (residual) layer (Figure 1c) [31]. The lithology is mainly composed of low-grade regional metamorphic rocks of continental and neritic facies, dominated by slate, sandstone, metasandstone, and marble. The stratum primarily has a monoclinic structure, and the strike is generally distributed in the south–north direction (SN) and the north–northeast (NNE) direction, with a dip of 260°–320°, and dip angles ranging from 47° to 85°. Partially due to the magmatic rock mass, it tends toward the northeast (NE) and southeast (SE) directions. The Indosinian felsic magmatic intrusive rocks are well-developed in this area, and mainly intrude into the second member (C_2m^2) of the Upper Carboniferous

Mengnan County Formation. In the study area, they are in the form of stock (or batholith) and distributed along the south–north (SN) or northeast (NE) direction [36]. The lithology is mainly monzodiorite, hornblende quartz monzonite, altered quartz monzodiorite, and diorite. The structure of the mining area is well-developed, primarily manifesting as crumple, fault, brittle–ductile shear zones, joint-fissure, etc. There are 16 main faults in the area, including 10 in the northeast (NE) direction, which form the phase I structure of the mining area, and 6 in the NW direction, which form the phase II structure of the mining area. Further, north–south and east–west concealed faults could exist, which control the intrusion of the main rock masses and large geological boundaries in the mining area. The second member of the Upper Carboniferous Mengnan County Formation (C_2m^2) is the main Au mineralization stratum in the mining area. The mineralized bodies are irregular in the vein, echelon and lenticular shape, and are closely related to faults and shear fracture zones (Figure 2).

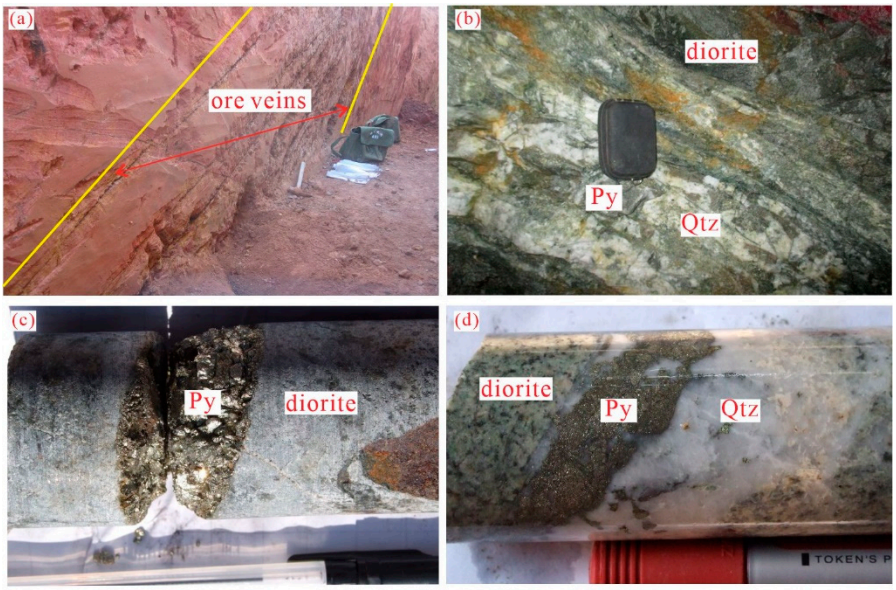


Figure 2. Characteristics of some mineralized bodies in the Sarakan Gold Deposit. (**a**) Ore veins of TC801, (**b**) quartz–sulfide vein in diorite, (**c**) pyrite occurred as massive aggregates in diorites, and (**d**) coexistence of pyrite and quartz in a hand sample. Py, pyrite; Qtz, quartz.

3.2. Geophysical Characteristics

The mineralization types that were found in the study area were mainly quartz-pyrite, complex vein-type gold deposits and structural fracture zone-iron, lead-zinc polymetallic skarn-type gold. As for the main ore-controlling factors for diorite rock and the structural fracture zone, the ore-rocks were mainly pyrite-bearing diorite, limonite, laterite-bearing limonite particles, quartz vein, tectonic breccia, and skarn, and the ore minerals were mainly pyrite, limonite, pyrrhotite, etc. In view of the above characteristics, we measured the physical parameters of the surface outcrop and borehole samples in the mining area (Tables 1 and 2).

According to the results in Tables 1 and 2, the magnetic strength of rocks (ore) in the study area was as follows: volcanic rock > sedimentary rock. Among them, the ore-bearing rocks (pyrite-bearing diorite and limonite) had the highest magnetic susceptibility and the strongest magnetic properties, while the sedimentary rocks (limestone, metamorphic siltstone, sandy slate, argillaceous slate, etc.) had the lowest magnetic susceptibility, and showed obvious weak magnetism. The electrical characteristics were as follows: the ore-bearing rocks (limonite and pyrite-bearing diorite) had the highest polarizability and strong electrical conductivity, and the sedimentary rocks (limestone, metamorphic siltstone, sandy slate, argillaceous slate) had the lowest polarizability and exhibited weak electrical conductivity.

Table 1. Magnetic parameters of the Sarakan Gold Deposit.

Lithology	Number	κ ($4\pi \times 10^{-6}$ SI)				Jr (10^{-3} A/m)				Remarks
		Minimum	Maximum	Average Value	Deviation	Minimum	Maximum	Average Value	Deviation	
Argillaceous slate	32	4.4	2747.0	401.8	736.7	7.2	124.4	44.8	30.6	Surface (specimen)
Marble	8	5.7	2300.2	618.5	983.4	2.9	89.4	25.9	30.8	
Diorite	32	2.6	505.2	95.4	100.6	9.7	910.1	126.6	184.6	
Pyrrhotite-bearing diorite	33	236.6	2849.9	1204.0	695.4	40.0	4396.4	565.6	863.2	
Limonite	31	8.1	16,528.5	1192.6	3095.0	24.3	612.8	214.2	123.6	
Limestone	32	0.1	4.6	1.4	1.2					Drilling (susceptibility meter)
Metamorphic siltstone	36	1.0	52.8	19.6	13.0					
Sandy slate	32	3.5	51.2	23.1	12.1					
Argillaceous slate	32	1.2	214.9	48.8	54.1					

Table 2. Electrical parameter determination in the Sarakan Gold Deposit.

Lithology	Number	M (%)				ρ (Ω·m)				Remarks
		Minimum	Maximum	Average Value	Deviation	Minimum	Maximum	Average Value	Deviation	
Carbonaceous mudstone	33	0.87	1.63	1.25	0.17	38.21	62.47	49.31	6.50	Surface (specimen)
Carbonaceous slate	31	1.04	2.37	1.64	0.32	78.48	833.46	270.38	162.20	
Limestone	31	1.07	2.67	1.87	0.45	162.07	15,668.47	5825.45	4828.42	
Diorite	45	2.06	3.83	2.95	0.38	955.11	4791.88	2750.92	1056.51	
Limonite	35	6.28	11.74	8.69	0.99	2130.77	26,823.74	7546.41	5304.80	
Sandy slate	32	0.16	2.99	1.53	0.74	1029.10	10,516.58	5581.23	2590.85	Drilling (IP instrument)
Metamorphic siltstone	37	0.24	3.64	1.76	0.94	4659.94	144,539.9	49,060.72	41,925.02	
Argillaceous slate	32	0.33	3.78	1.84	0.97	2072.29	32,497.32	15,204.00	9832.29	
Pyrrhotite-bearing diorite	20	4.023	15.05	7.78	3.67	11,961.7	76,119.5	32,108.6	19,686.2	

Therefore, there were differences in the magnetic susceptibility and polarization values between ore (or mineralized magmatic rocks) and the surrounding rock (or non-mineralized magmatic rocks) in the study area, which is a prerequisite for effective geophysical exploration. The results also showed that we can not only delineate the range of diorite and metal sulfide by the magnetic and IP methods, but also infer the morphology of the metallogenic structure.

4. Geophysical Survey

This study is based on the previous geological achievements of the study area and the general survey of gold deposits in the area in recent years (Figure 1). Firstly, we carried out a high-precision magnetic survey in the mining area to delineate the magnetic anomaly areas, magnetic minerals' (pyrrhotite, magnetite) structure, and the skarn zone. Secondly, the IP survey was carried out according to the important delineated magnetic anomalies, so as to delineate the IP anomaly area—the concentrated area of metal sulfides (pyrite)—and determine the favorable position of orebody enrichment. Finally, the transient electromagnetic method was carried out in the overlapping area of the delineated important magnetic and electrical anomalies to ascertain the shape, burial depth, and structural framework of the ore-controlling rock mass in the mining area, to provide a sufficient geological basis for design in deep-drilling engineering. At the same time, it also provides the best framework for discussing deep geological bodies within the study area. The geophysical exploration work was divided into the southern and northern mining areas.

The engineering layout, equipment parameters, and anomaly interpretation of different geophysical prospecting work methods are outlined below.

4.1. High-Precision Magnetic Measurement

A total of 6 GSM-19T proton precession magnetometers, imported from Canada GEM, were used in this high-precision magnetic measurement. The measurement parameter was the total value of the geomagnetic field (nT), the measurement range was 20,000–120,000 nT, the resolution was 0.01 nt, and the accuracy was 0.2 nT. The total base point of the survey was selected in the normal magnetic field, and the coordinates were: (x: 1,986,248.437, y: 782,535.6053, h: 196.753). The variation of the horizontal and vertical gradients of the magnetic field was less than 2 nT within the radius of 2 m and the height difference of 0.5 m, and there was no magnetic disturbance (especially mobile magnetic disturbance) nearby. According to the occurrence and morphology of the rock mass and the characteristics of the surrounding rock mass, 27 magnetic survey lines were arranged along the northwest–southeast (NW–SE) direction in the Sarakan Gold Deposit, coinciding with the geophysical survey line; at the same time, two high-precision magnetic survey sections were arranged in the south–north (SN) direction. Among them, the working network degree to the north of the mining area was 160 m × 20 m, and that to the south was 80 m × 20 m.

After correcting the data collected in the field magnetic survey by the total base point (theoretical field, T_0 = 44,060), daily variation, latitude, and gradient, the abnormal value, ΔT, of each measuring point was calculated to form a magnetic survey result table. Then, we used the Mapgis geographic information system to draw the ΔT profile plan and the ΔT contour map (Figure 3a,b). It can be seen from Figure 3a that the study area belongs to a strong magnetic field area, and the magnetic field intensity in the north and south mining areas were basically the same. Magnetic anomalies not only reflect the enrichment of magnetic substances in rocks, but also help us to understand the distribution law of magnetic substances deep underground. Due to the tectonic development in the study area and the close relationship between orebodies and faults, finding hidden faults can also help us find hidden orebodies (mineralization). Combined with the magnetic and geological characteristics of rocks and ores in the study area and their prospecting significance, four magnetic anomalies were circled from north to south, numbered C-1~C-4 (Figure 3b).

Among them, the southern mining area was generally a positive and negative C-1 magnetic anomaly, and the area of the positive anomaly in the magnetic survey area was much larger than the area of the negative anomaly. The magnetic field value gradient near the zero-value line of the magnetic anomaly greatly changed, and the high-value center appeared locally in the positive and negative magnetic anomaly areas, and the anomaly periphery was not closed. The ΔT was between –650 and 600 nT. It is speculated that the positive magnetic anomaly was caused by quartz monzodiorite, and the negative magnetic anomaly was caused by the metamorphic rock series of the second member of the Mengnan County Formation of Upper Carboniferous.

From the south to the north, the magnetic field in the north mining area showed a negative–positive–negative–positive–negative magnetic anomaly zone, consisting of three magnetic anomalies (C-2~C-4), and the C-3 magnetic anomaly was the major magnetic anomaly in this area. This anomaly was also associated with positive and negative anomalies, and the positive anomaly was dominant, with a wide and slow anomaly, and the positive anomaly area was larger than the negative anomaly area. The northern part of the anomaly area was mainly negative anomalies, while the southern part was mainly positive anomalies. The zero-value line was located near the 88 line. The anomaly was nearly 1600 m-long, 1100 m-wide, and 1.7 km^2 in area. The magnetic field intensity was large, and ΔT was between −600 and 400 nT. It is speculated that the magnetic anomaly is a comprehensive reaction of shallow orebodies (chemical) and deep magnetic bodies.

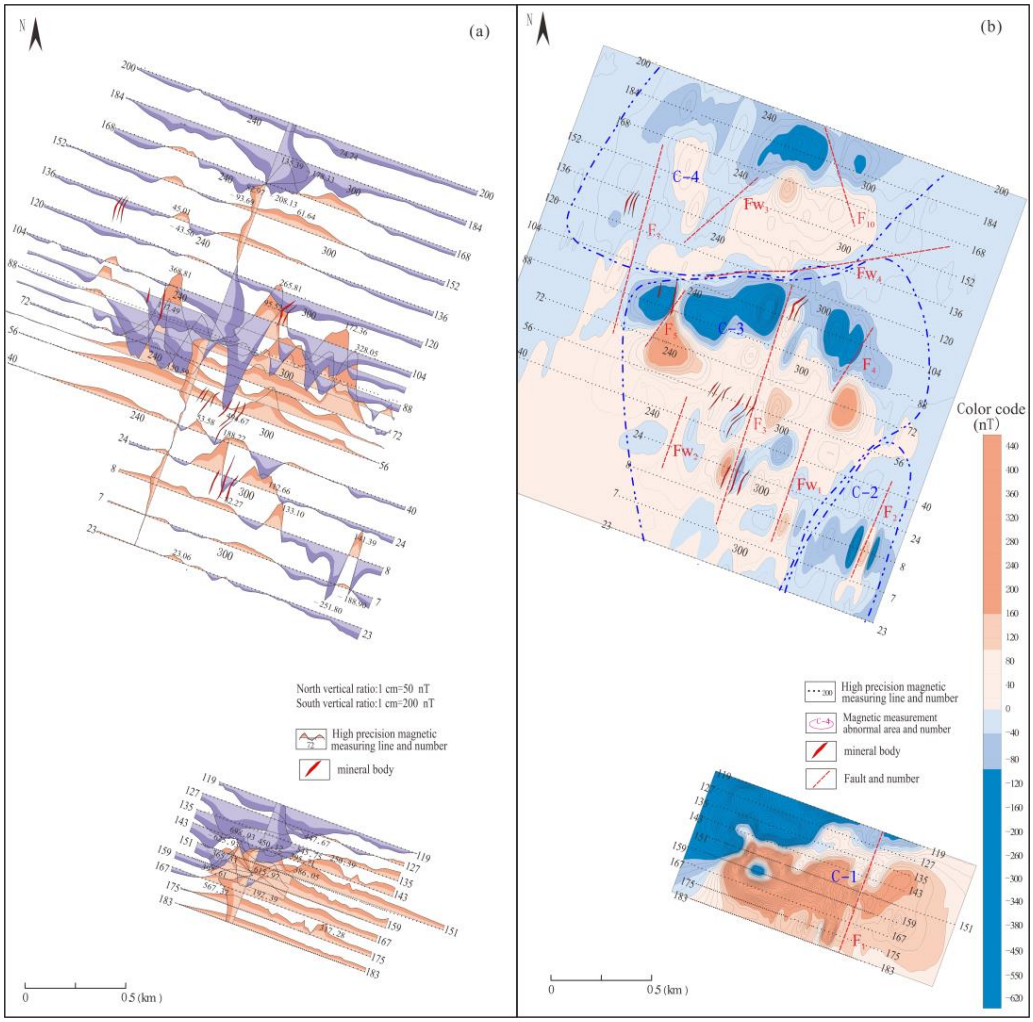


Figure 3. (**a**) High-precision magnetic measurement profile of the Sarakan Gold Deposit. (**b**) High-precision magnetic measurement, ΔT, isoline plan of the Sarakan gold-mining area (with magnetic anomaly range and number).

4.2. IP Measurement

These IP measurements were mainly used for IP middle-step scanning. An MDE6700 alternator produced by Mitsubishi Company of Japan was used as the power supply, a WDFZ-10 high-power intelligent transmitter, made in China, was also used in the power-supply system, and a WDJS-2 digital IP instrument was used for observation. The electrode distance AB = 1260 m, the point distance = 20 m, and the measuring pole distance MN = 40 m. The IP measurement line was arranged in the NW–SE direction, coincided with multiple magnetic measurement lines, and was cut at a large angle with the stratum occurrence or structural strike. A total of 27 IP mid-step sweeps were completed, over a length of 41.9 km.

Through the statistics and processing of the original observation values measured by the ladder-scanning surface in IP in the study area, after gridding, the isoline plan was drawn at a certain distance, the isoline in the local area was encrypted or diluted, and the abnormal map of IP measurement in the Sarakan gold mine was obtained (Figure 4a,b). The apparent resistivity (ρ_s) was calculated as follows: $\rho_s = K \times \Delta V_1/I$ (where K is the device coefficient, $K = 2\pi/(1/AM-1/AN-1/BM+1/BN)$, I is the supply current, and ΔV_1 is the primary field potential difference between MN). According to the charging rate (MS), the first integral M1 was used for editing and finishing, and the final picture was formed. It can be seen from Figure 4a that the background value of resistivity in the study area was

100–260 Ωm, and the abnormal peak value of resistivity in the south and north mining areas was basically the same. It can be seen from Figure 4b that there was a greater difference in the electric field between the northern mining area and the southern mining area (the apparent charging rate background value of the northern mining area was generally 8–9%, and the south mining area was 5.5–6.5%; the maximum value reached 17% in the northern mining area, and in the southern mining area the maximum value was 11.5%). Combined with the significance of geological prospecting and the proportion of anomaly delineation, the lower limit of anomaly in the north mining area was 10.0%, and that in the south mining area was 7.0%, respectively, to delineate the IP anomalies. A total of 7 IP anomalies were delineated here, and the anomaly numbers were IP-1~IP-7.

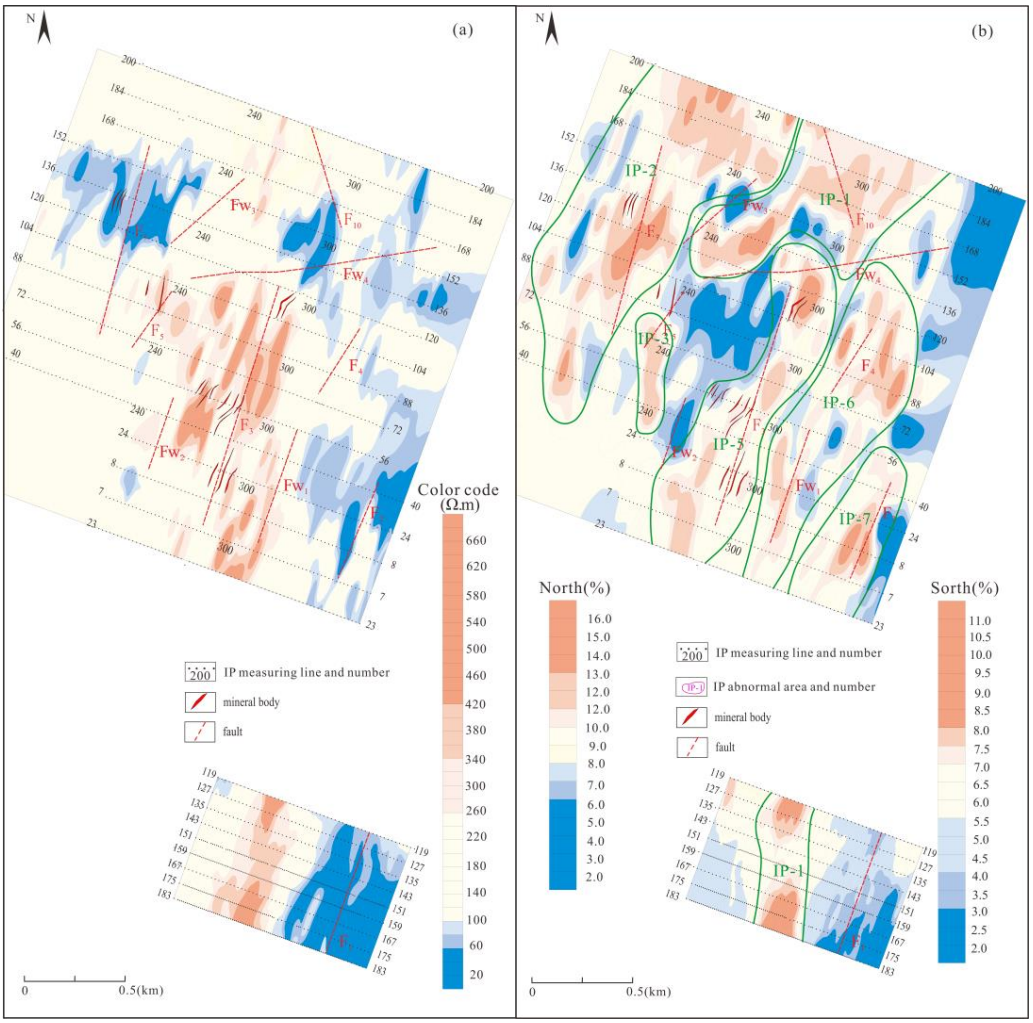


Figure 4. (**a**) Apparent resistivity isoline plan of IP measurement in the Sarakan Gold Deposit. (**b**) Apparent charging rate isoline plan of IP measurement in the Sarakan gold-mining area (with IP anomaly range and number attached).

Among them, the southern mining area mainly contained the IP-1 anomaly, which was located in the middle of the C-1 magnetic anomaly, and the corresponding magnetic field intensity, ΔT, was between −450 nT and 450 nT. The anomaly spread in a strip-like pattern in the north–south direction. The north and south ends of the anomaly were not closed. The high anomaly value was on the survey line at both ends, and the anomaly tended to increase from the inside to the outside. The anomaly length was greater than 650 m, the width was about 200 m, and the area was greater than 0.15 km^2. The anomalous intensity was relatively high, with a peak value of 11%. The north and south ends of the anomaly

were the middle- and high-resistance areas, and the corresponding apparent resistivity value was between 380 and 620 Ω·m.

The north mining area consisted of six IP anomalies (IP-2~IP-7), among which IP-3, IP-5, and IP-6 were closely related to the C-3 magnetic anomaly. The three anomalies are described in detail below:

(1) The IP-3 anomaly was located in the south-central part of the north mining area and overlapped with the positive magnetic anomaly section on the west side of the C-3 magnetic anomaly. The anomaly was oval in shape on the plane, spreading in the north–south direction, with a length of about 550 m, a width of 100 m, an area of about 0.05 km^2, and the highest anomaly value of 13.9%. The northern part of the anomaly was reflected as a medium–high-resistance area, and the apparent resistivity value was about 320 Ω·m. The IP anomaly was located in the north and south stopes of the mine, with orebodies numbered Au4-1, Au4-2, and Au4-3. The abnormal trend is consistent with the known orebodies. The local high magnetic anomaly was assumed to be caused by the known orebodies and slag. Combined with the geological metallogenic conditions, it is speculated that the IP-3 anomaly was caused by the part of the known orebodies extending southward, and the geological body (mineralized body) causing the anomaly was buried 90~180 m deep.

(2) The IP-5 anomaly was located in the southern part of the north mining area, overlapping with the central part of the C-3 magnetic anomaly. The anomaly was strip-shaped and bead-shaped on the plane, in the NNE–SSW direction, consistent with the known orebody group. The anomaly was longer than 1600 m and 200–400 m-wide. The anomaly was not closed to the southwest, with an area of about 0.45 km^2. The anomaly had four lenticular high-value areas, with a peak height of 16.9%, generally 10~13%. The three high-value abnormal areas of the apparent charging rate to the south of the anomaly area were located in the positive magnetic anomaly, and the high-value abnormal area of the apparent charging rate in the north was located in the negative magnetic anomaly. At the same time, the anomaly was reflected as a high-resistance area on the apparent resistivity value plan as a whole, and the peak apparent resistivity was about 660 Ω·m.

(3) The IP-6 anomaly was located in the central and eastern parts and overlapped with the eastern part of the C-3 magnetic anomaly. The anomaly was generally elongated on the plane, composed of multiple vein-like and lens-like small anomalies, the direction was NE–SW, and the intensity of the anomaly in the north was greater than that in the south. The anomaly was about 1300 m-long, 200 m-wide, and 0.2 km^2 in area, with high strength and a peak value of 16.7%. The northeast of the abnormal area was a medium-resistance area, and the southwest was a medium- and high-resistance area, and the corresponding apparent resistivity value was about 240–600 Ω·m. At the same time, the high-value anomaly area of this anomaly showed a significant positive magnetic anomaly. Combined with the characteristics of the known orebodies with medium and high resistance and a strong magnetic field, it is speculated that the anomaly was caused by shallow metal sulfides.

4.3. Transient Electromagnetic Measurement

The transient electromagnetic survey can be carried out in the important magnetic anomalies and electrical anomalies delineated by the high-precision magnetic survey and the DC IP survey, which can be used to predict the ore-controlling rock mass and structural morphology. For this transient electromagnetic measurement, we used the GEONIS PROTEM transient electromagnetic system imported from Canada, which uses a central loop device and a wire synchronization method to observe the vertical component of the secondary potential. The side length of the power supply loop is 80 × 80 m, the power supply wire is a 2.5 mm^2 multi-core copper wire, and the receiving coil is a high-frequency 1D coil. The operating frequency is 25 Hz, the power supply current is >10 A, the down-delay turn-off time is 30 μs, the gain is 1, the integration time is 15 s, and the

number of sampling channels is 30. At the same time, the observation point and line number, the power supply current, the voltage, frequency, gain, integration time, power-off delay, storage number, and the geological conditions were recorded.

The measurement data were transmitted from the instrument to the computer for format conversion, data-filtering processing, calculation of the whole process of apparent resistivity, time–depth conversion, and other processing and analyses, and then we used surfer8.0 for inversion inference. A total of 10 transient electromagnetic survey profiles with a length of 16.67 km were completed, and the characteristics of the inverted resistivity sections of each profile were roughly similar. Their electrical characteristics objectively reflected the vertical and lateral changes and extensions of the underground rock formations and structures. The inversion results of the two main transient electromagnetic measurement lines in the north and south mining areas are described below (Figure 5).

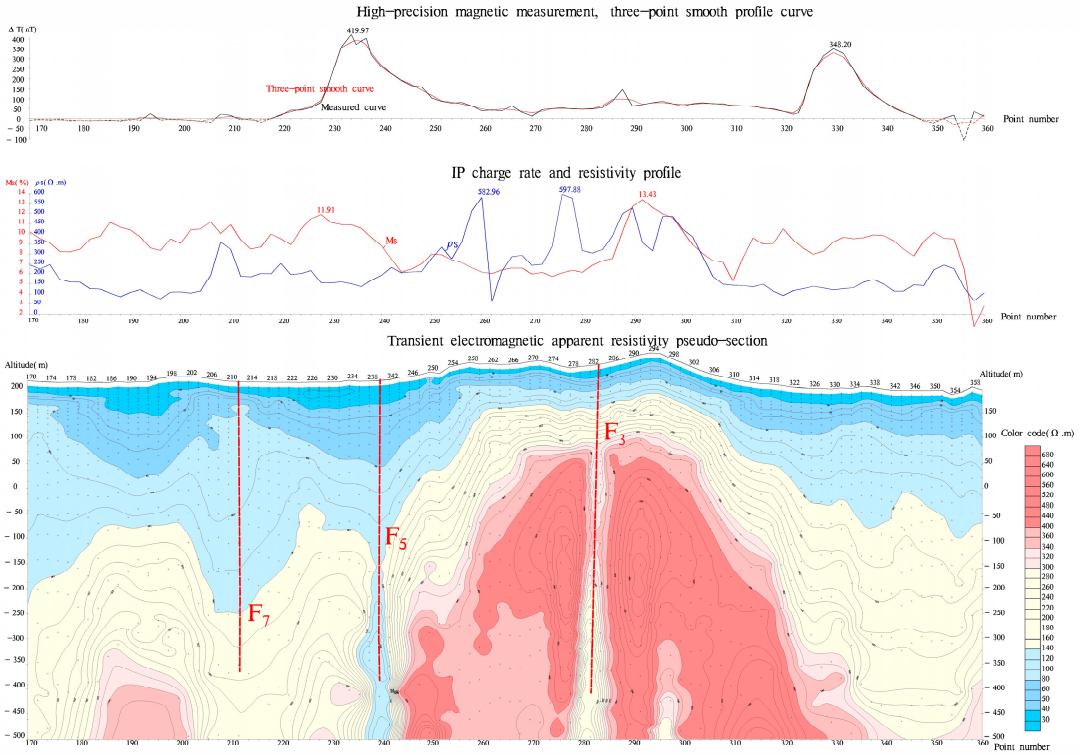


Figure 5. The 72-line transient electromagnetic sounding resistivity pseudo-section map.

Line 72 was located in the north mining area and passed through the main magnetic anomaly area (C-3) and three IP anomaly areas (IP-3, IP-5, and IP-6). According to the inversion results of transient electromagnetic sounding (Figure 5), there was an obvious high-resistance anomaly area at the depth of 150–550 m, with a double-kidney shape in the plane, which was presumed to be a magmatic rock mass. The faults F_3, F_5, and F_7, with a NW tendency, were identified in the area of the double-kidney junction in the high-resistivity abnormal area and in the area of the steep change zone of resistivity in the west. These faults strictly control the shape of the deep rock mass.

Line 151 was located in the south mining area, passing through the main magnetic anomaly area (C-1) and the main IP anomaly area (IP-1). According to the inversion results of transient electromagnetic sounding (Figure 6), there was an obvious elliptical high-resistance anomaly in the southwest corner, and the resistivity value increased with the increase in depth, which was presumed to be a magmatic rock mass. The top of the concealed rock mass was about 200 m away from the ground and extended downward for more than 500 m. A fault, F1, was identified along the resistivity gradient tight-transition zone in the east, the fault was inclined to the northwest, and the dip angle gradually

decreased as the depth increased, strictly controlling the shape of the rock mass in the southwest corner.

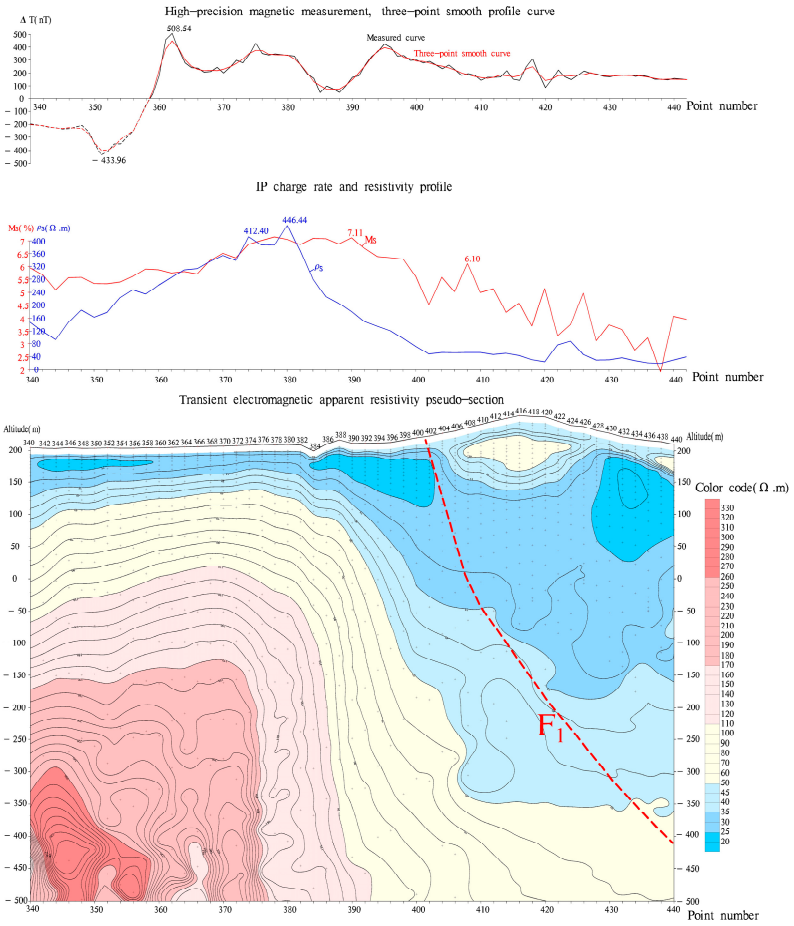


Figure 6. The 151-line transient electromagnetic sounding resistivity pseudo-section map.

5. Results and Discussion

The genetic type of the deposit in the study area was mainly the quartz pyrite vein-type gold deposit occurring in the brittle–ductile shear structure of the intermediate-acid magmatic rocks in Indosinian, and the intrusive activities of the intermediate-acid magmatic rocks were strictly controlled by the late structures. At the same time, combined with the results of this geophysical and surface geological survey, we believe that high magnetism, high polarization, and medium–high resistance are the signs pointing to concealed mineralization bodies in the study area, which provided the best framework for us to discuss the deep geological bodies in the study area.

5.1. Magmatic Rocks

Indosinian felsic rocks were mainly developed in the study area, and the lithology was primarily composed of monzodiorite, hornblende quartz diorite, altered quartz monzodiorite, and diorite. The analysis results of the rocks are shown in Table 3. The SiO_2 contents of the Sarakan samples ranged between 62.28 wt% and 68.71 wt%. In the TAS and QAP diagrams (Figure 7a), the samples are plotted in the granodiorite-diorite area. In the SiO_2-K_2O rock series diagram (Figure 7b), the rock belongs to the sho-shone high-potassium calc-alkaline series. K_2O/Na_2O was 2.59–5.18, with an average of 3.71, which belonged to the rock mass formed by the deep melting of continental crust sediments. The diorite rock was generally characterized by medium–high resistivity, medium–high polarizability, and strong magnetism, and five diorite bodies were delineated (inferred) here (Figure 8).

Table 3. Major elements' data of the Sarakan Gold Deposit.

Number	HQ2	HQ2	HQ3	HQ4	HQ5	HQ6	HQ7	HQ8	HQ9
SiO_2	63.71	62.28	67.15	63.46	68.71	66.81	64.86	68.13	64.74
TiO_2	0.48	0.71	0.53	0.41	0.51	0.26	0.24	0.33	0.56
Al_2O_3	11.56	11.16	12.25	11.52	12.14	11.68	10.43	10.47	11.14
Fe_2O_3	9.43	5.11	5.94	12.10	6.50	9.66	12.05	9.44	8.21
FeO	0.85	0.57	0.71	0.52	0.54	0.97	0.39	0.38	0.87
MnO	0.05	0.06	0.04	0.05	0.06	0.07	0.03	0.02	0.04
MgO	0.91	1.43	0.94	0.76	1.00	0.47	0.48	0.55	1.44
CaO	1.18	0.40	0.85	0.83	0.55	0.44	0.34	0.28	2.55
Na_2O	0.89	0.60	1.81	0.86	0.96	1.36	0.88	0.91	1.33
K_2O	4.43	4.57	3.81	3.11	4.69	3.66	3.72	3.29	4.33
P_2O_5	0.12	0.04	0.07	0.09	0.04	0.10	0.14	0.10	0.10
SO_2	0.38	0.06	0.13	0.07	0.05	0.13	0.25	1.03	2.19
LOI	4.82	7.99	4.18	5.86	4.15	4.26	5.83	5.00	2.48
DI	73.68	79.52	79.93	69.66	80.11	76.85	74.19	76.97	72.52
SI	5.71	11.95	7.31	4.6	7.52	3.03	2.87	3.86	9.18
A/NK	1.85	1.88	1.72	2.41	1.82	1.88	1.91	1.95	1.62
A/CNK	1.51	1.72	1.47	1.92	1.62	1.77	1.8	1.87	1.31
AR	2.43	2.62	1.76	1.95	2.61	2.41	2.44	2.29	2.41
σ	1.29	1.23	1.26	0.72	1.21	1.02	0.92	0.78	1.43

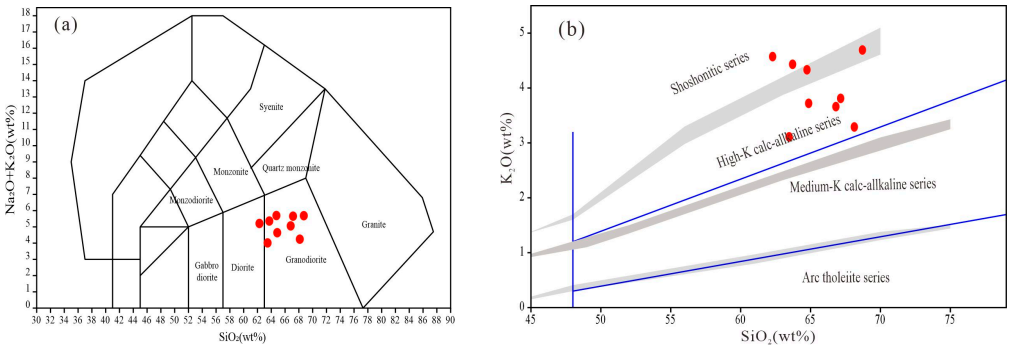


Figure 7. Major element diagrams of the Sarakan diorite pluton. (**a**) Total alkali versus silica diagram [38]. (**b**) SiO_2 vs. K_2O diagram [39]. Data sources for the Sarakan Gold Deposit are from [40].

Based on the characteristics of the geology, ore-controlling structure, and ore mineral alteration combination, it was inferred that the magnetic anomaly in the south mining area was caused by quartz monzonite diorite, and the contact interface between the rock mass and the surrounding rock mass was near the zero-value line of the magnetic measurement. The trend of the zero-value line of the magnetic anomaly in the north mining area was nearly east–west, and the trend of the local magnetic anomaly was only south–north, which is consistent with the trend of the known gold vein. It is speculated that the magnetic anomaly was caused by the local shallow orebody. The intensity at both ends of the magnetic anomaly was lower than that in the middle section, and it is speculated that the magnetic anomaly was mainly caused by the quartz vein-type gold vein group and the pyrite-bearing rock mass, which was relatively large in area, which is beneficial to delineate the ore-bearing geological body. The results of the IP survey generally showed that the amplitude of the apparent charging rate in the north mining area was higher than that in the south mining area, and several abnormal areas with high values in the north and south mining areas were consistent with the known orebodies (veins). It is speculated that the IP anomaly was mainly caused by the shallow–middle gold deposit (mineralization) body and the fault alteration zone, which is of great significance to the search for oxidized gold deposits and surface engineering construction in the shallow part of the present study area.

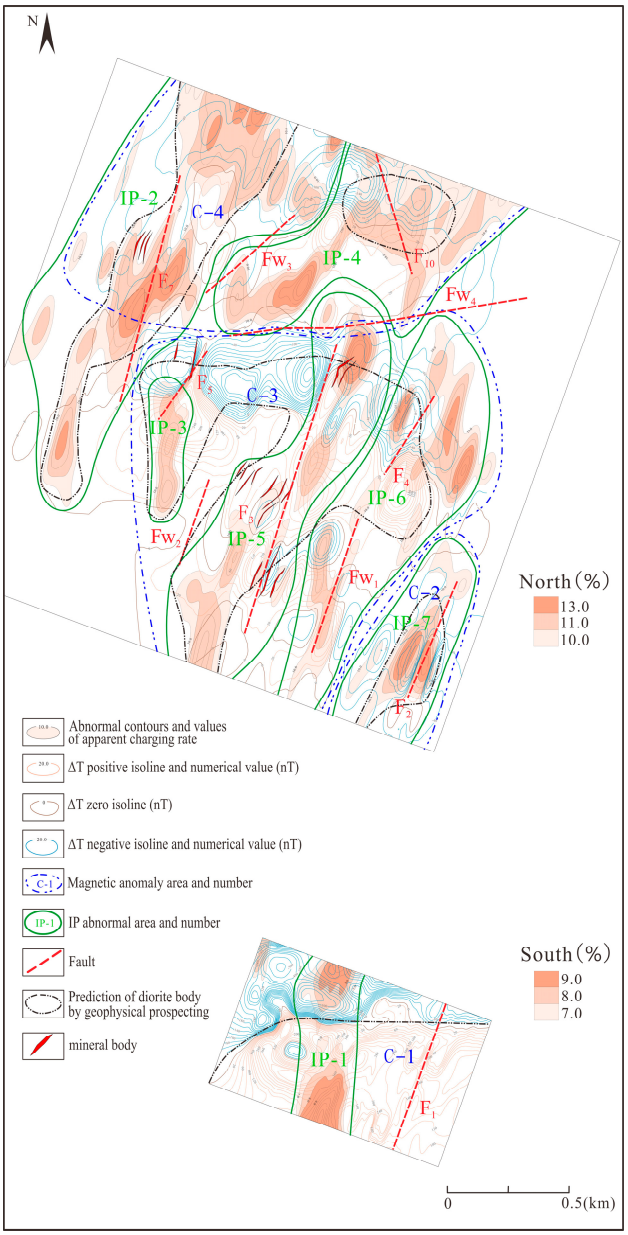


Figure 8. Comprehensive anomaly map of the geophysical survey of the Sarakan gold mine.

5.2. Metallotectonics

According to the results of the high-precision magnetic survey and the transient electromagnetic survey, combined with the geological data, it was found that the structure in the study area was extremely developed, and had the characteristics of multi-phase and inherited activities. The regional data showed that, influenced by two hyper-lithospheric fault zones (Figure 1b), the main tectonic framework in the study area was NE-trending, followed by NW-trending. The tectonic traces appeared as faults, cataclastic rock zones, brittle–ductile shear fracture alteration zones, etc., and were mainly distributed near the contact zone between the intermediate-acid magmatic rock mass and the strata. The NE-trending faults were the main faults in the mining area, and these faults were relatively large in scale, had a long extension length, and had developed fracture zones and strong silicification.

In this magnetic measurement, linear structures and cracks were well-identified in the boundary zone of the positive and negative magnetic anomalies, and 11 faults were circled, including 4 inferred concealed faults (Figure 3b), while the electromagnetic method

used in the gradient tight-resistivity transition zone could better identify the regional deep-fracture characteristics (Figures 5 and 6). Based on ten transient electromagnetic measurement profiles in the north and south mining areas, three-dimensional profiles of the main metallogenic structures in the study area were drawn (Figures 9 and 10). It can be seen from Figure 9 that the delineated concealed rock mass in the south mining area was mainly distributed in the southwest corner, with a depth of more than 500 m, which was strictly controlled by the F1 fault, structurally, and the buried depth showed a gradient decline from the SW to the NE. The F_1 fault was the main structure of the south mining area: the exposed length was more than 3 km, it was generally inclined to the northwest and locally inclined to the east, the inclination angle was 31–85°, and the inclination angle gradually decreased as the depth increased. It can be seen from Figure 10 that the delineated concealed rock mass in the north mining area was mainly distributed in the central and southern parts, with good north–south continuity, and its outcropping morphology was mainly controlled by deep faults. The size of the rock mass developed from the north to the south, which first increased and then decreased, and it reached the maximum at the position of line 72. The main structure in the north mining area was a NE-trending fault, and the largest exposed fault was the F3 fault. The outcrop length of the fault was close to 1.5 km, and it was generally inclined to the northwest, with a dip angle of 45–78°. On the east and west sides of the fault, there were faults F_5, F_7, F_{w2}, and F_{w3} with a SE trend and F_2, F_4, and F_{w4} with a NW trend. These faults strictly controlled the shape of the deep magmatic rock mass.

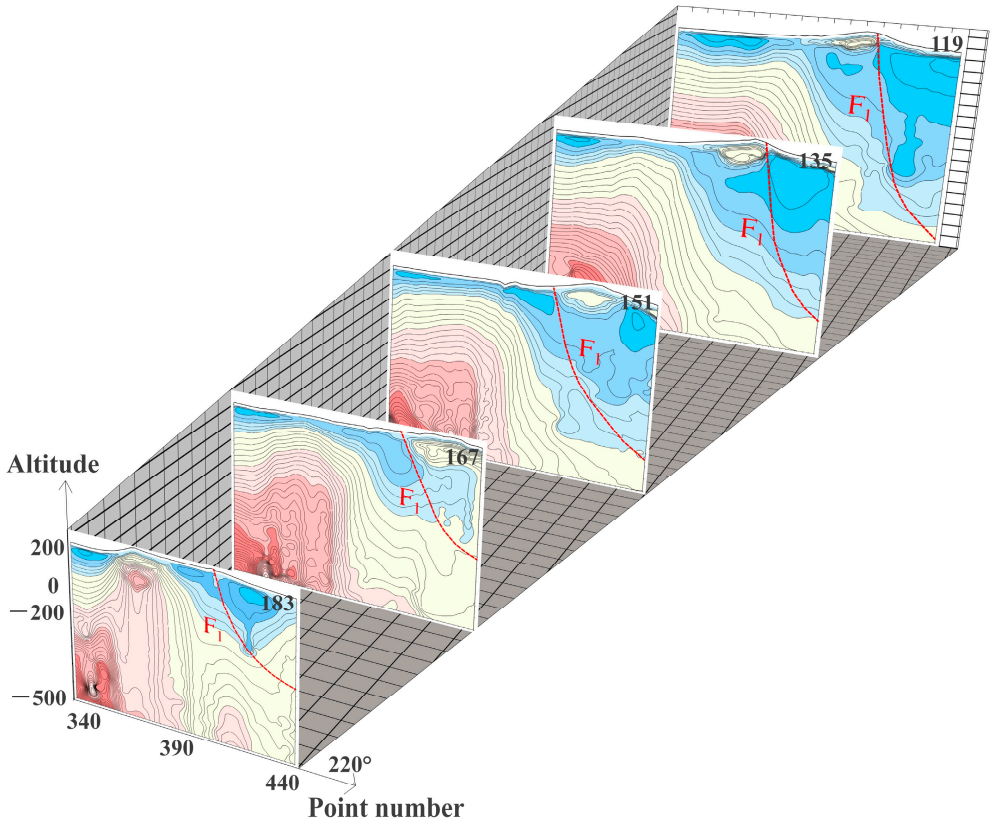


Figure 9. Comparison of transient electromagnetic 3D sections in the south mining area.

Combined with the regional geology and the comprehensive geophysical exploration results, it was inferred that these faults were formed in the early Indosinian period, and they are the channels for the upwelling of deep magmatic rocks, controlling the intrusion of the main rock bodies and the larger geological boundary of the mining area. It was inferred that these faults are the ore-guiding and ore-hosting structures of the deposit.

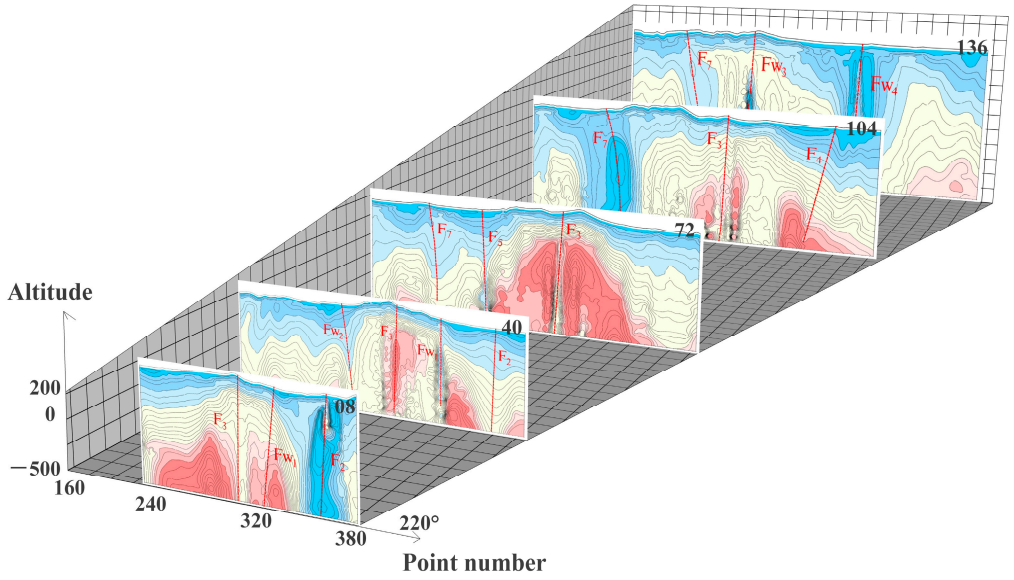


Figure 10. Comparison of transient electromagnetic 3D sections in the north mining area.

5.3. Mineralization Model of the Sarakan Deposit

On the basis of the geophysical survey, exploration trenches and drilling were used for engineering verification. We found that the orebodies were mainly hosted in quartz pyrite and quartz pyrrhotite veins of diorite, monzodiorite, monzonite, and slate. The orebodies were not controlled by lithology and were mostly located at the intersection of multiple groups of faults. Generally, they were in a nearly north–south direction, and the tilt direction was eastward. The orebodies were mainly vein-shaped, with some of them manifesting as irregular lenses.

Therefore, we proposed a conceptual metallogenic model to describe the metallogenic process (Figure 11). During the Indosinian period, under the influence of collision and amalgamation between the Simao–Phitsanuluo micro-block and the Vientiane–Kunsong block, the deep layers of the crust were remelted to form felsic magmatic rocks, which intruded into the Carboniferous sandstone slate along the NE or nearly EW direction. This formed a large number of NE-trending faults or shear zones. At the same time, some minerals were activated and initially enriched along the structure. The oceanic crust that was being subducted had no chance to raise its temperature to the high range of the surrounding mantle due to its low temperature and quick subduction pace. Strong changes in temperature and pressure produced metamorphic fluid by dehydration and decarbonization, as well as the initial ore-forming fluid by mixing deep magmatic fluid. The Luang Prabang fault and the Preshan fault were created as a result of the back-arc basin of the Nan-Uttaradit subducting to the east during the Late Permian–Early Triassic. This process also caused lithospheric delamination and thinning. The thickened lower crust was created as a result of the asthenosphere mantle magma rising to the surface [34]. Continuous sinking causes the deep asthenosphere's material to vigorously up-well, which further produces a lot of heat energy and causes the crust to remelt, resulting in the formation of a mixed fluid of crust and mantle. Large-scale magmatic intrusion causes the lithospheric mantle to be continually thinned and depleted, which causes metallogenetic elements (such as Au, Cu, and others) to be removed from the upper mantle and move upward through the mantle plume. The components that compose ore were extracted as a result of the ore-bearing fluid's intense reaction with the wall rock as it ascended. The metamorphic fluid rich in gold and other minerals was immiscible and phase-separated from the post-felsic magmatic-hydrothermal solution in the mining area due to the change in tectonic properties (ductile→ductile–brittle→brittle), which led to the precipitation and enrichment of ore-forming materials in the structural fracture alteration zone formed in the

early stage (Figure 11). This model has provided new insights for the metallogenic research and exploration of the Sarakan Deposit and the entire Luang Prabang–Loei island arc belt.

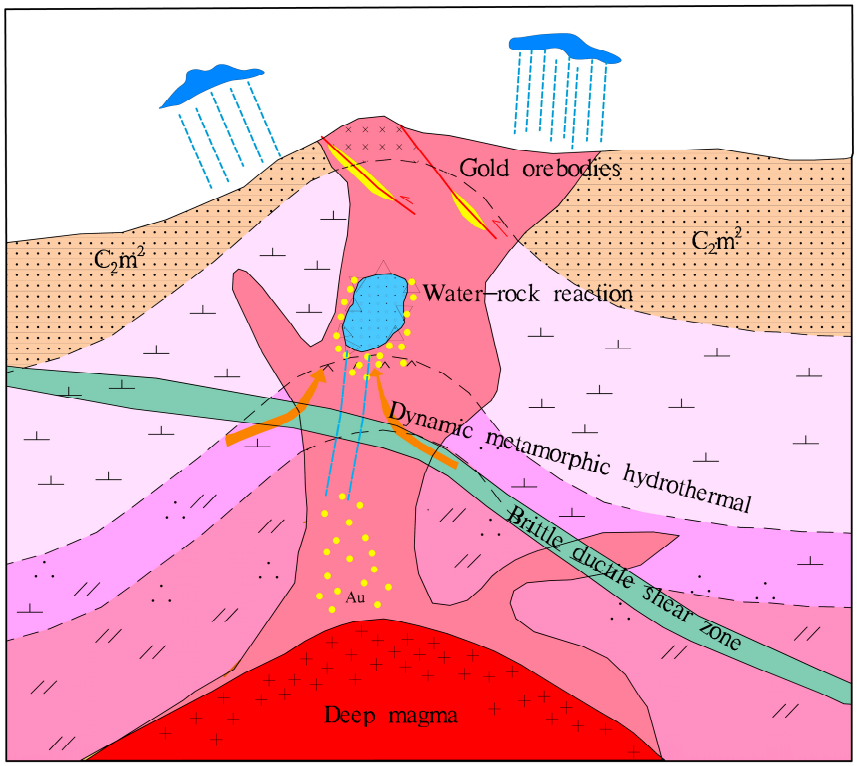


Figure 11. Ore-forming model diagram of the Sarakan Gold Deposit.

In summary, the ore deposits in the intensive ore belt of the study area were closely related to the Indosinian felsic magmatic intrusive body and significantly controlled by their fault structure. The results of this comprehensive geophysical exploration are in good agreement with the drilling verification results, which shows that the comprehensive geophysical method is effective for use.

6. Conclusions

(1) The genetic type of the Sarakan Gold Deposit in Laos was found to be mainly the quartz (magnetite)-pyrite vein-type, which occurred in the brittle–ductile shear structure near the contact zone between the magmatic rock and the surrounding rock. It is closely related to the Indosinian felsic magmatic intrusive body and is obviously controlled by the fault structure.

(2) Through the use of magnetic, electrical, and geological methods, the relationship between the tectonic framework and the metallogenic structure in the study area was determined, and the geophysical prospecting criteria in this area were found to be high-magnetic, high-polarization, and medium–high-resistivity geophysical anomaly areas. The NE-trending fault zone in the study area was the ore-guiding and ore-hosting structure. The intersection of these faults provided the primary metallogenic space and trap conditions. The ore deposits were highly altered and concentrated in terms of mineralization. It is obvious that the structure is an important indicator when searching for such deposits.

(3) When comparing trenching, drilling, and other geological survey data with the results of geophysical anomalies, the results were found to be highly consistent. The reliability of the results of the magnetic and electrical methods was verified, which indicates that they are useful for exploring the relationship between mineralization, magmatic rock masses, and the structure.

(4) The geophysical anomaly characteristics and prospecting experience in the study area can provide guidance and effective geophysical exploration methods for finding similar deposits in the Luang Prabang–Loei island arc.

Author Contributions: H.L., J.G. and Y.G. designed the project; H.L. and B.W. performed the original literature reviews; Y.L. and W.J. performed the field geological survey; H.L. and J.G. wrote and organized the paper, with a careful discussion and revision by Y.G. All authors have read and agreed to the published version of the manuscript.

Funding: This research project is jointly funded by the mineral resources risk exploration project of the Sarakan gold deposit in Sarakan County, Vientiane Province, Laos (2019) and the land and resources survey project of the China Geological Survey (1212011120337).

Data Availability Statement: The experimental data used to support the conclusions of this study are included within the article.

Acknowledgments: The authors are thankful for the support of Laos Guanghang Mining Co., Ltd. We also thank the 7th geological team of the Sichuan Provincial Bureau of Geology and Mineral Resources for their technical field support.

Conflicts of Interest: The authors declare no conflict of interest.

References

1. Alfouzan, F.; Zhou, B.; Bakkour, K.; Alyousif, M. Detecting near-surface buried targets by a geophysical cluster of electromagnetic, magnetic and resistivity scanners. *J. Appl. Geophys.* **2016**, *134*, 55–63. [CrossRef]
2. Guo, X.; Gao, J.; Zhang, D.; Li, J.; Xiang, A.; Li, C.; Wang, S.; Jiao, T.; Ren, C. Genesis of the Erdaohe skarn Pb-Zn-Ag deposit in the Great Hinggan Range, NE China: Evidence from geology, fluid inclusions, and H–O–S isotope systematics. *Ore Geol. Rev.* **2022**, *140*, 104414. [CrossRef]
3. Xie, F.; Tang, J.; Chen, Y.; Lang, X. Apatite and zircon geochemistry of Jurassic porphyries in the Xiongcun district, southern Gangdese porphyry copper belt: Implications for petrogenesis and mineralization. *Ore Geol. Rev.* **2018**, *96*, 98–114. [CrossRef]
4. Zhang, Y.; Liu, K.; Wang, Y.; Zhang, D.; Mo, X.; Deng, Y.; Yu, T.; Zhao, Z. Geological Significance of Late Permian Magmatic Rocks in the Middle Section of the Ailaoshan Orogenic Belt, SW China: Constraints from Petrology, Geochemistry and Geochronology. *Minerals* **2022**, *12*, 652. [CrossRef]
5. Cheng, M.; Yang, D.; Luo, Q. Interpreting Surface Large-Loop Time-Domain Electromagnetic Data for Deep Mineral Exploration Using 3D Forward Modeling and Inversion. *Minerals* **2023**, *13*, 34. [CrossRef]
6. Lv, H.; Xu, L.; Yang, B.; Su, P.; Xu, H.; Wang, H.; Yao, C.; Su, P. Mineralization Based on CSAMT and SIP Sounding Data: A Case Study on the Hadamengou Gold Deposit in Inner Mongolia. *Minerals* **2022**, *12*, 1404. [CrossRef]
7. Han, S.; Wang, S.; Tang, Z.; Tan, K.; Duan, X.; He, H.; Feng, Z.; Xie, Y. Integrated geophysical exploration of the coupling of a concealed rock body and metallogenic structures—Ag-Pb-Zn mining area case study in Jilinbaolige, Inner Mongolia, China. *J. Appl. Geophys.* **2020**, *178*, 104048. [CrossRef]
8. Gan, J.; Li, H.; He, Z.; Gan, Y.; Mu, J.; Liu, H.; Wang, L. Application and Significance of Geological, Geochemical, and Geophysical Methods in the Nanpo Gold Field in Laos. *Minerals* **2022**, *12*, 96. [CrossRef]
9. He, J. Combined Application of Wide-Field Electromagnetic Method and Flow Field Fitting Method for High-Resolution Exploration: A Case Study of the Anjialing No. 1 Coal Mine. *Engineering* **2018**, *4*, 667–675. [CrossRef]
10. Li, J.; Wang, Y.; Zhu, C.; Xue, X.; Qian, K.; Xie, X.; Wang, Y. Hydrogeochemical processes controlling the mobilization and enrichment of fluoride in groundwater of the North China Plain. *Sci. Total Environ.* **2020**, *730*, 138877. [CrossRef]
11. Olajide-Kayode, J.O.; Mustapha, S.O.; Olatunji, A.S.; Okunlola, O.A. Assessment of gold mineralisation in Osu–Amuta–Itagunmodi areas, Southwestern Nigeria. *Arab. J. Geosci.* **2020**, *13*, 573. [CrossRef]
12. Sono, P.; Nthaba, B.; Shemang, E.M.; Kgosidintsi, B.; Seane, T. An integrated use of induced polarization and electrical resistivity imaging methods to delineate zones of potential gold mineralization in the Phitshane Molopo area, Southeast Botswana. *J. Afr. Earth Sci.* **2020**, *174*, 104060. [CrossRef]
13. Wilson, C.J.L.; Moore, D.H.; Vollgger, S.A.; Madeley, H.E. Structural evolution of the orogenic gold deposits in central Victoria, Australia: The role of regional stress change and the tectonic regime. *Ore Geol. Rev.* **2020**, *120*, 103390. [CrossRef]
14. Zeng, Q.; Di, Q.; Liu, T.; Li, G.; Yu, C.; Shen, P.; Liu, H.; Ye, J. Explorations of gold and lead-zinc deposits using a magnetotelluric method: Case studies in the Tianshan-Xingmeng Orogenic Belt of Northern China. *Ore Geol. Rev.* **2020**, *117*, 103283. [CrossRef]
15. Liu, S.; Guo, L.; Ding, J.; Hou, L.; Xu, S.; Shi, M.; Liang, H.; Nie, F.; Cui, X. Evolution of Ore-Forming Fluids and Gold Deposition of the Sanakham Lode Gold Deposit, SW Laos: Constrains from Fluid Inclusions Study. *Minerals* **2022**, *12*, 259. [CrossRef]
16. Kwan, K.; Müller, D. Mount Milligan alkalic porphyry Au–Cu deposit, British Columbia, Canada, and its AEM and AIP signatures: Implications for mineral exploration in covered terrains. *J. Appl. Geophys.* **2020**, *180*, 104131. [CrossRef]

17. Shi, M.; Lin, F.; Fan, W.; Deng, Q.; Cong, F.; Tran, M.; Zhu, H.; Wang, H. Zircon U–Pb ages and geochemistry of granitoids in the Truong Son terrane, Vietnam: Tectonic and metallogenic implications. *J. Asian Earth Sci.* **2015**, *101*, 101–120. [CrossRef]
18. Zaw, K.; Meffre, S.; Lai, C.; Burrett, C.; Santosh, M.; Graham, I.; Manaka, T.; Salam, A.; Kamvong, T.; Cromie, P. Tectonics and metallogeny of mainland Southeast Asia—A review and contribution. *Gondwana Res.* **2014**, *26*, 5–30.
19. Qian, X.; Feng, Q.; Wang, Y.; Chonglakmani, C.; Monjai, D. Geochronological and geochemical constraints on the mafic rocks along the Luang Prabang zone: Carboniferous back-arc setting in northwest Laos. *Lithos* **2016**, *245*, 60–75. [CrossRef]
20. Chen, H.; Chen, Y.; Baker, M. Isotopic geochemistry of the Sawayaerdun orogenic-type gold deposit, Tianshan, northwest China: Implications for ore genesis and mineral exploration. *Chem. Geol.* **2012**, *310–311*, 1–11. [CrossRef]
21. Goldfarb, R.J.; Taylor, R.D.; Collins, G.S.; Goryachev, N.A.; Orlandini, O.F. Phanerozoic continental growth and gold metallogeny of Asia. *Gondwana Res.* **2014**, *25*, 48–102. [CrossRef]
22. Huo, F.; Wang, X.; Wen, H.; Xu, W.; Huang, H.; Jiang, H.; Li, Y.; Li, B. Genetic mechanism and pore evolution in high quality dolomite reservoirs of the Changxing-Feixianguan Formation in the northeastern Sichuan Basin, China. *J. Petrol. Sci. Eng.* **2020**, *194*, 107511. [CrossRef]
23. Shifeng, W.; Yasi, M.; Chao, W.; Peisheng, Y. Paleotethyan evolution of the Indochina Block as deduced from granites in northern Laos. *Gondwana Res.* **2016**, *38*, 183–196.
24. Sun, T.; Chen, F.; Zhong, L.; Liu, W.; Wang, Y. GIS-based mineral prospectivity mapping using machine learning methods: A case study from Tongling ore district, eastern China. *Ore Geol. Rev.* **2019**, *109*, 26–49. [CrossRef]
25. Yang, X.; Zaw, K.; Bin Ghani, A. Preface for the special issue "Magmatism, tectonic evolution and metallogenesis in SE Asia and the adjacent region". *Ore Geol. Rev.* **2021**, *129*, 103890. [CrossRef]
26. Shi, M.; Khin, Z.; Liu, S.; Xu, B.; Meffre, S.; Cong, F.; Nie, F.; Peng, Z.; Wu, Z. Geochronology and petrogenesis of Carboniferous and Triassic volcanic rocks in NW Laos: Implications for the tectonic evolution of the Loei Fold Belt. *J. Asian Earth Sci.* **2021**, *208*, 104661. [CrossRef]
27. Wang, Y.; Yang, T.; Zhang, Y.; Qian, X.; Gan, C.; Wang, Y.; Wang, Y.; Senebouttalath, V. Late Paleozoic back-arc basin in the Indochina block: Constraints from the mafic rocks in the Nan and Luang Prabang tectonic zones, Southeast Asia. *J. Asian Earth Sci.* **2020**, *195*, 104333. [CrossRef]
28. Hou, L.; Liu, S.; Guo, L.; Xiong, F.; Li, C.; Shi, M.; Zhang, Q.; Xu, S.; Wu, S. Geology, Geochronology, and Hf Isotopic Composition of the Pha Lek Fe Deposit, Northern Laos: Implications for Early Permian Subduction-Related Skarn Fe Mineralization in the Truong Son Belt. *J. Earth Sci.-China* **2019**, *30*, 109–120. [CrossRef]
29. Guo, L.; Hou, L.; Liu, S.; Nie, F. Rare Earth Elements Geochemistry and C–O Isotope Characteristics of Hydrothermal Calcites: Implications for Fluid-Rock Reaction and Ore-Forming Processes in the Phapon Gold Deposit, NW Laos. *Minerals* **2018**, *8*, 438. [CrossRef]
30. Yang, W.; Qian, X.; Feng, Q.; Shen, S.; Chonglakmani, C. Zircon U-Pb geochronological evidence for the evolution of the Nan-Uttaradit suture in northern Thailand. *J. Earth Sci.-China* **2016**, *27*, 378–390. [CrossRef]
31. Zhao, T.; Qian, X.; Feng, Q. Geochemistry, zircon U-Pb age and Hf isotopic constraints on the petrogenesis of the Silurian rhyolites in the Loei fold belt and their tectonic implications. *J. Earth Sci.-China* **2016**, *27*, 391–402. [CrossRef]
32. Zhang, Z.; Shu, Q.; Wu, C.; Zaw, K.; Cromie, P.; von Dollen, M.; Xu, J.; Li, X. The endogenetic metallogeny of northern Laos and its relation to the intermediate-felsic magmatism at different stages of the Paleotethyan tectonics: A review and synthesis. *Ore Geol. Rev.* **2020**, *123*, 103582. [CrossRef]
33. Bounliyong, P.; Itaya, T.; Arribas, A.; Watanabe, Y.; Wong, H.; Echigo, T. K–Ar geochronology of orogenic gold mineralization in the Vangtat gold belt, southeastern Laos: Effect of excess argon in hydrothermal quartz. *Resour. Geol.* **2021**, *71*, 161–175. [CrossRef]
34. Li, H.; Gan, J.; He, Z.; Gan, Y.; Wang, B.; Li, Y.; Jiang, W. Petrogenesis and Geodynamic Significance of the Early Triassic Nanpo Adakitic Pluton of the Luang Prabang-Loei Tectonic Belt (Northwestern Laos) in the East Tethys Domain: Constraints from Zircon U-Pb-Hf Isotope Analyses and Whole-Rock Geochemistry. *Minerals* **2023**, *13*, 821. [CrossRef]
35. Long, Y.; Zhang, D.; Huang, D.; Yang, X.; Chen, S.; Bayless, R.C. Age, composition and tectonic implications of late Ordovician-early Silurian igneous rocks of the Loel Volcanic Belt, NW Laos. *Int. Geol. Rev.* **2019**, *61*, 1940–1956. [CrossRef]
36. Zou, H.; Han, R.; Liu, M.; Cromie, P.; Zaw, K.; Fang, W.; Huang, J.; Ren, T.; Wu, J. Geological, geophysical, and geochemical characteristics of the Ban Kiouchep Cu–Pb–Ag deposit and its exploration significance in Northern Laos. *Ore Geol. Rev.* **2020**, *124*, 103603. [CrossRef]
37. Li, Y.; Hou, Z.; Li, M.; Wang, C.; Liu, X.; Li, S. Soil Geochemical Characteristics and Significance of the Shalakan Gold Deposit in Laos. *Mod. Min.* **2021**, *37*, 16–21. (In Chinese)
38. Middlemost, E.A.K. Naming materials in the magma/igneous rock system. *Earth-Sci. Rev.* **1994**, *37*, 215–224. [CrossRef]
39. Peccerillo, A.; Taylor, S.R. Geochemistry of eocene calc-alkaline volcanic rocks from the Kastamonu area, Northern Turkey. *Contrib. Mineral. Petr.* **1976**, *58*, 63–81. [CrossRef]
40. Li, Y. Geological Characteristics and Genesis of Sanakham Gold Deposit in Vientiane Province, Laos. Master's Thesis, Chengdu University of Technology, Chengdu, China, 2022. (In Chinese).

Disclaimer/Publisher's Note: The statements, opinions and data contained in all publications are solely those of the individual author(s) and contributor(s) and not of MDPI and/or the editor(s). MDPI and/or the editor(s) disclaim responsibility for any injury to people or property resulting from any ideas, methods, instructions or products referred to in the content.